

Real-Time Motion Generation and Control Systems for High Wheel-Legged Robot Mobility

Akihiro Suzumura and Yasutaka Fujimoto, *Senior Member, IEEE*

Abstract—A wheel-legged mobile robot (WLMR) has both leg and wheel structures. WLMRs have adaptability advantages because they can change locomotion methods depending on the terrain. However, the location of a WLMR's center of gravity (CoG) is very high; thus, almost all existing WLMRs move statically. In this paper, whole body motion generation and various control systems are studied to facilitate higher WLMR mobility. To this end, a zero moment point (ZMP) is introduced as a stability index. In addition, WLMRs are modeled as single point mass linear inverted pendulums. Subsequently, online CoG pattern generation methods are proposed; one is a preview control approach, and a second is an approach that realizes the desired ZMP pattern using a zero-phase low-pass filter. It is then possible to generate the desired CoG patterns more easily and faster than with a preview control approach. The CoG patterns based on the single point model are constructed via the resolved-momentum-control approach. Finally, the effectiveness of the whole body motion pattern generated by the proposed methods is validated by simulations and experiments.

Index Terms—Center of gravity (CoG) pattern generation, hybrid mobile robot, resolved momentum control (RMC), wheel-legged mobile robot (WLMR), zero moment point (ZMP), zero-phase low-pass filter (ZPLPF).

I. INTRODUCTION

IN THE NEAR future, robots will be expected to execute a variety of tasks in diverse environments. In particular, security, rescue, and life-assist robots have attracted considerable attention. To meet those expectations, wheel-legged mobile robots (WLMRs) that have both leg and wheel structures have been developed [1]–[13]. There are many types of WLMR mechanisms, and almost all of them have the following favorable features: 1) stair locomotion and obstacle avoidance via a multi-degree-of-freedom (DoF) leg mechanism and 2) a high energy efficiency wheel mechanism. From the aforementioned features, WLMRs have the advantages of legged and wheeled mobile robots. In addition, they have a significant mobility and adaptability advantage because they can change locomotion methods depending on the terrain. For these reasons, WLMRs have many applications, including as rovers on uneven terrain and human-assist robots for environmental adaptation. In our

study, we focus on WLMR applications for human-assist purposes [14]. Adaptability is one of the most important factors in human-assist robots because these robots are required to adapt to a variety of environments. In addition, the speed of motion is also important. Because moving robots are at risk of colliding with humans, they require sufficient agility to avoid such collisions. Moreover, mobile robots that follow humans (e.g., luggage-carrying robots) should be capable of keeping up with the humans [15]. Therefore, in addition to being adaptable, it is required that WLMRs be quick and agile.

In this paper, we focus on 3-D WLMRs [16], [17]. The center of gravity (CoG) of such robots is inevitably quite high. Thus, there is a constant risk of falling over. Therefore, almost all 3-D WLMRs move statically and exhibit only adaptability. To obtain high mobility, the zero moment point (ZMP), which is generally used as a stability index for bipedal robots [18]–[20], is applied to the 3-D WLMR. It is anticipated that the ZMP-based 3-D WLMR will move faster and more stably than the conventional 3-D WLMR.

There have been several studies that focused on increasing the speed and stability of robots such as rovers [21] and mobile manipulators [22], [23]. In addition, An *et al.* investigated ways of increasing the speed of WLMRs on the basis the ZMP [13]. They realized the ZMP control of a WLMR by feedforward (FF) and feedback compensation using a precise dynamical model. This approach needs the explicit formulas of the dynamical model. However, the number of DoFs of the robot increased, complicating the situation. Furthermore, their approach was validated for only 2-D simulations, and no validation experiments were conducted. On the contrary, we achieved whole body motion generation and high mobility control based on the approach similar to the case of biped robots. More specifically, the WLMR is approximated as a single point mass linear inverted pendulum (LIP). Then, the CoG pattern that produces the desired ZMP pattern is generated. A preview controller is usually used to generate the CoG pattern online [24], [25]. In this paper, we proposed two CoG pattern generation methods for WLMR; the first is a method based on a preview control, and the other is a method based on a zero-phase low-pass filter (ZPLPF). The ZPLPF can generate the CoG pattern more easily and faster than the preview controller. The effectiveness of these proposed methods is validated based on the root-mean-square error (RMSE) of ZMP tracking results. Next, the generated CoG pattern is realized by the resolved momentum control (RMC) system [30]. The RMC approach enables a robot to control its linear momentum and angular momentum around the CoG. The linear momentum Jacobian used in RMC includes the CoG Jacobian [26], [27]. The robot's

Manuscript received October 9, 2012; revised March 16, 2013 and July 22, 2013; accepted September 4, 2013. Date of publication October 17, 2013; date of current version January 31, 2014.

A. Suzumura was with the Department of Electrical and Computer Engineering, Yokohama National University, Yokohama 240-8501, Japan. He is now with Denso Corporation, Ltd., Aichi 448-8661, Japan.

Y. Fujimoto is with the Department of Electrical and Computer Engineering, Yokohama National University, Yokohama 240-8501, Japan (e-mail: fujimoto@ynu.ac.jp).

Color versions of one or more of the figures in this paper are available online at <http://ieeexplore.ieee.org>.

Digital Object Identifier 10.1109/TIE.2013.2286071

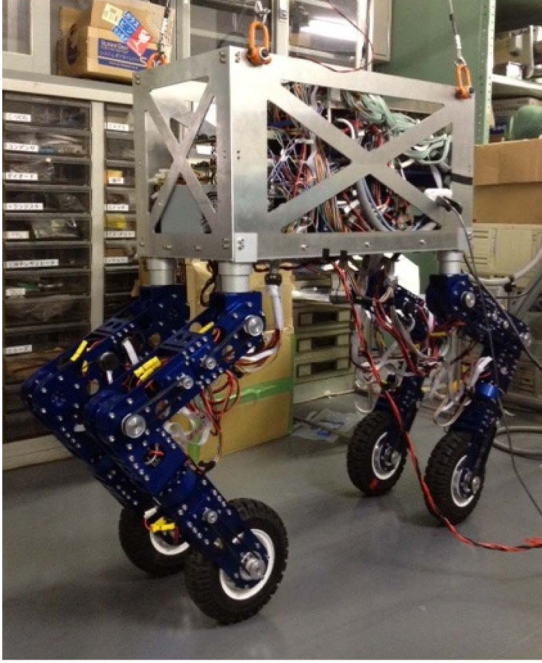


Fig. 1. Overview of the experimental setup.

CoG then follows the desired CoG pattern. In addition, the angular momentum is another important factor used to achieve high robot mobility. There are several studies on ZMP stabilizing control using an ankle joint [28], [29]. However, unlike humanoid robots, WLMRs generally do not have ankle joints and therefore cannot stabilize the ZMP using ankle joints. Nevertheless, further enhancement of the WLMR mobility with ZMP stabilization is expected by directly manipulating the angular momentum [30]–[32]. As an example, the posture of the WLMR can be controlled using the angular momentum as a control input. The angular momentum of the robot around the CoG can be manipulated using RMC to yield the desired value. Then, our motion generation method was implemented, and 3-D simulations and experiments were conducted to prove its effectiveness.

The content of this paper is organized as follows. In Section II, a WLMR model is developed. In Section III, we propose a CoG pattern generation method using a ZPLPF. In Section IV, a whole body motion generation scheme based on RMC is described. In Section V, the overall WLMR control system is outlined. In Section VI, our methods are validated via simulations and experiments. Finally, the conclusions are listed in Section VII.

II. ROBOT MODELING

This section deals with WLMR kinematic modeling. The robot is shown in Fig. 1. A computer aided design (CAD) view of the leg is in Fig. 2 and its link parameters are listed in Table I. The 3-D robot model and coordinate systems are depicted in Figs. 3 and 4. Each coordinate frame is defined as follows:

- 1) Σ_w : coordinates of the world;
- 2) Σ_B : coordinates of the base link;
- 3) Σ_{c_i} : coordinates of the wheel contact point.

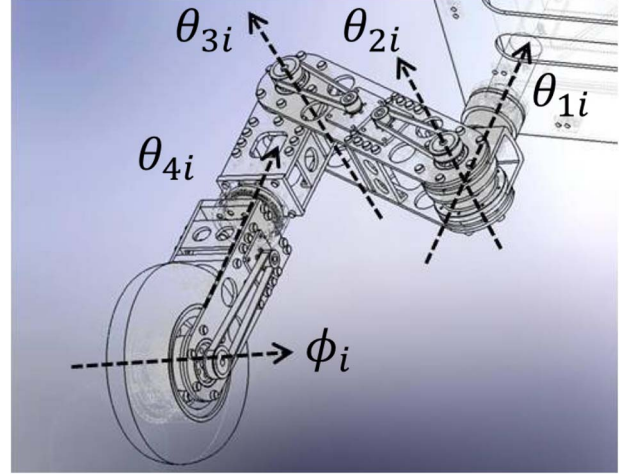


Fig. 2. CAD view of the leg mechanism.

TABLE I
LINK PARAMETERS

	Mass [kg]	Length [m]
Base	12.0	0.70(W) \times 0.35(D) \times 0.40(H)
Crotch	0.700	0.150
Thigh	3.03	0.350
Calf	1.52	0.140
Shin	1.61	0.280
Wheel	1.88	0.104

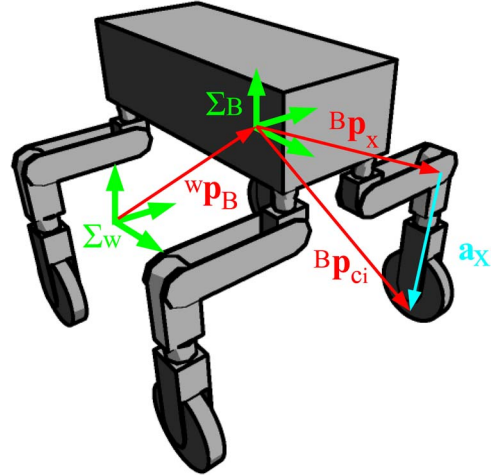


Fig. 3. Three-dimensional robot model.

Then,

- 1) ${}^x \mathbf{p}_y \in \mathbb{R}^3$ is the position vector of the origin of Σ_y with respect to Σ_x ;
- 2) ${}^x \boldsymbol{\omega}_y \in \mathbb{R}^3$ and ${}^x \mathbf{R}_y \in \mathbb{R}^{3 \times 3}$ are the angular velocity and rotation matrix of Σ_y with respect to Σ_x .

The following statements are true. The relationship between ${}^x \boldsymbol{\omega}_y$ and ${}^x \mathbf{R}_y$ can be expressed as

$${}^x \dot{\mathbf{R}}_y = {}^x \boldsymbol{\omega}_y^\wedge \cdot {}^x \mathbf{R}_y \quad (1)$$

where \wedge is an operator that transforms a 3×1 vector into a 3×3 skew symmetric matrix equivalent to the cross product. Operator \vee is defined as the inverse of \wedge . In this way, the cross product can be rearranged into various forms,

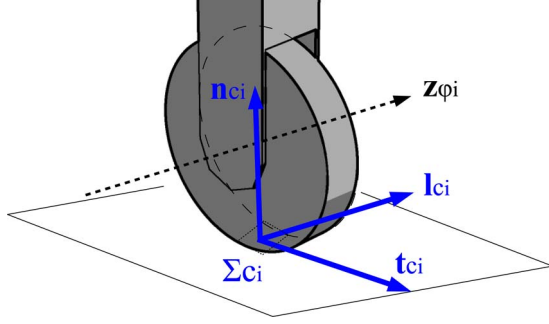


Fig. 4. Contact surface is assumed to be sufficiently stiff and flat.

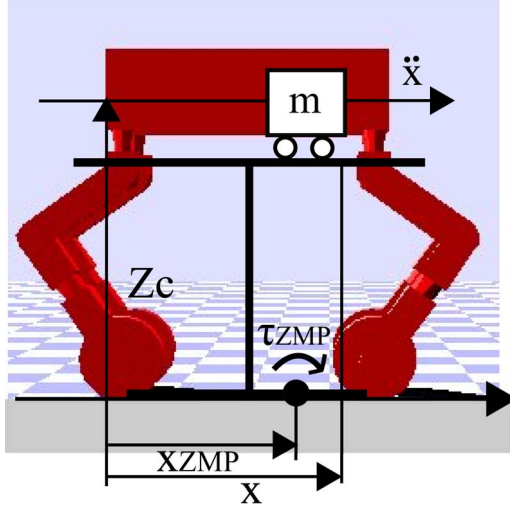


Fig. 5. Cart-table model.

i.e., $\mathbf{a}(\in \mathbb{R}^3) \times \mathbf{b}(\in \mathbb{R}^3) = -\mathbf{b} \times \mathbf{a} = -\mathbf{b}^\wedge \mathbf{a} = \mathbf{a}^\wedge \mathbf{b}$. Other kinematic variables are defined as follows.

- 1) $\phi = [\phi \ \theta \ \psi]^T$, and ϕ , θ , and ψ are the roll, pitch, and yaw angles expressed in terms of Euler angles.
- 2) $\theta_{legi} = [\theta_{1i} \ \theta_{2i} \ \dots \ \theta_{(n-1)i}]^T$ are the vectors containing the joint angles. n is the number of DoFs of the leg.

For our robot, $\theta_{legi} = [\theta_{1i} \ \theta_{2i} \ \theta_{3i} \ \theta_{4i}]^T$. $\theta_{1i} \sim \theta_{4i}$ are the crotch yaw, crotch roll, knee roll, and shin yaw joint rotation angle. The wheel rotation angle is denoted as ϕ_i , where i represents the index of the leg and each joint angle vector is summarized as $\theta_i = [\theta_{legi}^T \ \phi_i^T]^T \in \mathbb{R}^n$.

III. CoG TRAJECTORY GENERATION

A. LIP/Cart-Table Model

In our method, a cart-table model is adopted [24]. The conceptual model is shown in Fig. 5, where we consider the x -axis as the ordinal moving direction. In this model, the relationship between the CoG and ZMP is written as

$$x_{zmp} = x - \frac{z_c}{g} \ddot{x} \quad (2)$$

where z_c is the height of the cart's CoG, g is the gravitational acceleration, x is the CoG coordinate, and x_{zmp} is the ZMP coordinate; (2) is called the ZMP equation.

B. Preview Control Approach

The preview control approach was originally proposed by Kajita *et al.* in [24] as a CoG trajectory generation method for humanoid robots. In this paper, we propose the use of this method for the CoG trajectory generation of WLMRs. Details of this method are described as follows.

First, (2) is translated into a state-space expression as follows:

$$\frac{d}{dt} \begin{bmatrix} x \\ \dot{x} \\ \ddot{x} \end{bmatrix} = \begin{bmatrix} 0 & 1 & 0 \\ 0 & 0 & 1 \\ 0 & 0 & 0 \end{bmatrix} \begin{bmatrix} x \\ \dot{x} \\ \ddot{x} \end{bmatrix} + \begin{bmatrix} 0 \\ 0 \\ 1 \end{bmatrix} u \quad (3)$$

$$x_{zmp} = \begin{bmatrix} 1 & 0 & -\frac{z_c}{g} \end{bmatrix} \begin{bmatrix} x \\ \dot{x} \\ \ddot{x} \end{bmatrix} \quad (4)$$

where control input u is the time derivative of \ddot{x} . Equations (3) and (4) are then discretized with the sampling time Δt as follows:

$$\mathbf{x}[k+1] = \mathbf{A}_d \mathbf{x}[k] + \mathbf{B}_d u[k] \quad (5)$$

$$x_{zmp}[k] = \mathbf{C}_d \mathbf{x}[k] \quad (6)$$

where

$$\mathbf{x}[k] \equiv [x(k\Delta t) \ \dot{x}(k\Delta t) \ \ddot{x}(k\Delta t)^T]$$

$$u[k] \equiv u(k\Delta t)$$

$$x_{zmp}[k] \equiv x_{zmp}(k\Delta t)$$

$$\mathbf{A}_d = \begin{bmatrix} 1 & \Delta t & \frac{\Delta t^2}{2} \\ 0 & 1 & \Delta t \\ 0 & 0 & 1 \end{bmatrix}, \quad \mathbf{B}_d = \begin{bmatrix} \frac{\Delta t^3}{6} \\ \frac{\Delta t^2}{2} \\ \Delta t \end{bmatrix}$$

$$\mathbf{C}_d = \begin{bmatrix} 1 & 0 & -\frac{z_c}{g} \end{bmatrix}. \quad (7)$$

Next, we aim to minimize the cost function, which is written as follows:

$$J = \sum_{k=-N_L+1}^{\infty} (Q_e e[k]^2 + \Delta \mathbf{x}^T[k] Q_x \Delta \mathbf{x}[k] + R \Delta u[k]^2) \quad (8)$$

where $e[k] = x_{zmp}^{\text{ref}}[k] - x_{zmp}[k]$ is the ZMP tracking error at step k and $x_{zmp}^{\text{ref}}[k]$ is the ZMP reference. Q_e , Q_x , and R are the weighting coefficients for regulating each term of the cost function. Then, the optimal control input $u[k]$ that minimizes the cost function is given by

$$u[k] = F_e \sum_{j=0}^k e[j] + F_x \mathbf{x}[k] + \sum_{j=1}^{M_R} \mathbf{F}_R[j] x_{zmp}^{\text{ref}}[k+j] \quad (9)$$

where F_e , F_x , and $\mathbf{F}_R[j]$ are the feedback gains and preview gains calculated from Q_e , Q_x , R , and z_c/g based on preview control theory.

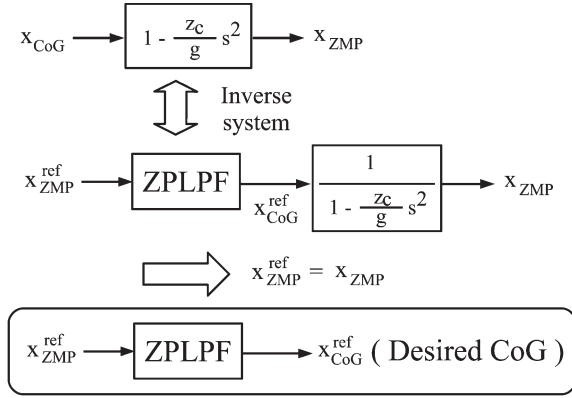


Fig. 6. Outline of the ZPLPF approach.

C. Inverse System Construction Using ZPLPF

In (2), let us define the input as the n th differential of the CoG, $p_{CoG}^{(n)}(t)$, and the output as the n th differential of the ZMP, $p_{zmp}^{(n)}(t)$. Then, the transfer function and frequency transfer function are expressed as follows:

$$G_p(s) = \frac{s^n P_{zmp}(s)}{s^n P_{CoG}(s)} \quad (10)$$

$$= 1 - \frac{z_c}{g} s^2 \quad (11)$$

$$G_p(j\omega) = 1 + \frac{z_c}{g} \omega^2 \quad (12)$$

where $P_{zmp}(s) = \mathcal{L}[p_{zmp}(t)]$ and $P_{CoG}(s) = \mathcal{L}[p_{CoG}(t)]$. We now focus on the frequency transfer function of the controlled plant. This system clearly has the characteristics of a zero-phase high-pass filter (ZHPF). The ZHPF characteristics can be canceled by a ZPLPF used as a FF compensator, as described in [36]. The details of the design of the ZPLPF in the discrete time domain are explained in [37]. We define (12) as the controlled plant and the ZPLPF as the FF compensator in the discrete time domain. Then, the characteristics of the controlled plant are perfectly canceled, and the ZMP pattern $p_{zmp}^{(n)}$ follows the reference pattern. The ZMP reference $p_{zmp}^{(n)}$ through the ZPLPF is equivalent to the desired CoG pattern $p_{CoG}^{(n)}$ because the control input is defined as the CoG pattern $p_{CoG}^{(n)}$. An outline of the ZPLPF approach is shown in Fig. 6. Later, we will show that the method can generate the desired CoG trajectory by feeding the target ZMP trajectory into the ZPLPF. Thereafter, the actual ZMP will follow the reference ZMP. We will also show that the ZPLPF can easily generate the CoG trajectory.

D. FIR-ZPLPF Design

In this section, the design method of the FIR-ZPLPF is described in detail. The general equation of the FIR-ZPLPF is given by

$$G_{FIR}[z, z^{-1}] = \alpha_0 + \sum_{k=1}^N \alpha_k (z^k + z^{-k}). \quad (13)$$

This filter can be divided into a causal filter $G[z]$ and a non-causal filter $G[z^{-1}]$, which are described as follows:

$$G_{FIR}[z, z^{-1}] = a_0 + \sum_{k=1}^N a_k (z^{-k}) + a_0 + \sum_{k=1}^N a_k (z^k) \quad (14)$$

$$= G[z] + G[z^{-1}] \quad (15)$$

where the filter coefficients of $G[z]$ and $G[z^{-1}]$ in (14) are identical. Thus, only the filter coefficients of the causal filter $G[z]$ need to be designed. The noncausal filter $G[z^{-1}]$ can be realized by assuming that the input signal for the future M th step value is known.

Next is about the derivation of the FIR-ZPLPF coefficient. The desired filter characteristic (transfer function) is the inverse system of the controlled plant

$$G_{ZPLPF}(s) = \frac{1}{G_p(s)} = \frac{1}{1 - T^2 s^2} \quad (16)$$

where $T = \sqrt{z_c/g}$. This transfer function can be written in the form

$$G_{ZPLPF}(s) = \frac{1}{2} \left(\frac{1}{1 + Ts} + \frac{1}{1 - Ts} \right). \quad (17)$$

Let us now compare the above equation with (15). Then, the following transfer function is chosen as an analog prototype filter:

$$G(s) = \frac{1}{1 + Ts}. \quad (18)$$

Thus, we obtain an finite impulse response (FIR) digital filter identical to filter (16). Next, the selected analog prototype filter $G(s)$ is discretized by the Tustin method with the sampling time equal to Δt

$$G[z] = \frac{1 + z^{-1}}{1 + \frac{2T}{\Delta t} + (1 - \frac{2T}{\Delta t}) z^{-1}}. \quad (19)$$

Subsequently, we calculate the impulse response of $G[z]$ as

$$\Lambda = [\delta_0 \ \delta_1 \ \delta_2 \ \cdots \ \delta_N] \quad (20)$$

where $\delta_n (n = 0, 1, 2, \dots)$ is the value at time $t = n\Delta t$. The various impulse responses of $G[z]$ are shown in Fig. 7. Next, we evaluate the following equation:

$$\tilde{a}_k = \sum_{k=1}^M \delta_n \delta_{n-k} \quad (21)$$

and derive the coefficient a_k using the following equation:

$$a_k = \frac{\tilde{a}_k}{\tilde{a}_0 + 2(\tilde{a}_1 + \tilde{a}_2 + \cdots + \tilde{a}_N)}. \quad (22)$$

Following these procedures, the desired ZPLPF is calculated from (15). Further details can be found in [36] and [37]. N is the number of points until the impulse response has converged.

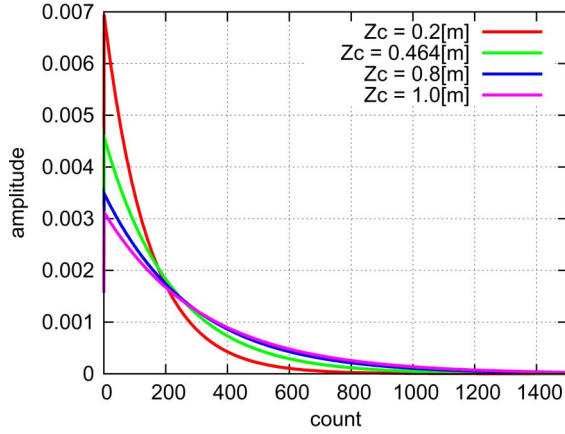


Fig. 7. Impulse response of the analog filter.

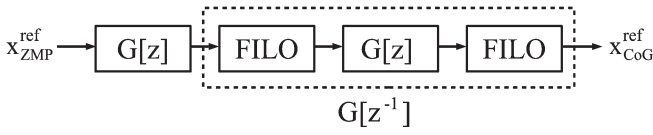


Fig. 8. Implementation of IIR-ZPLPF.

E. IIR-ZPLPF Design

Here, we describe the design method of the IIR-ZPLPF. The general equation of the IIR-ZPLPF is described as follows:

$$G_{\text{IIR}}[z, z^{-1}] = \frac{\sum_{i=0}^N \beta_i (z^i + z^{-i})}{1 + \sum_{k=0}^N \alpha_k (z^k + z^{-k})}. \quad (23)$$

This filter can be divided into a causal filter $G[z]$ and noncausal filter $G[z^{-1}]$ as follows:

$$G_{\text{IIR}} = \frac{\sum_{i=0}^N b_i (z^{-i})}{1 + \sum_{k=0}^N a_k (z^{-k})} \cdot \frac{\sum_{i=0}^N b_i (z^i)}{1 + \sum_{k=0}^N a_k (z^k)} \quad (24)$$

$$= G[z] \cdot G[z^{-1}] \quad (25)$$

where the coefficients of $G[z]$ and $G[z^{-1}]$ are coincident, which is similar to the FIR-ZPLPF case. Therefore, only the design coefficients of the causal filter $G[z]$ are needed. $G[z^{-1}]$ can be composed using the first-in-last-out (FILO) method [38]. Hence, the structure of the IIR-ZPLPF can be described as shown in Fig. 8, and the characteristics of the given IIR filter are identical to (16).

Next is about the derivation of the IIR-ZPLPF coefficient. The transfer function of the desired filter is given as

$$G_{\text{ZPLPF}}(s) = \frac{1}{1 - T^2 s^2} = \frac{1}{1 + Ts} \cdot \frac{1}{1 - Ts}. \quad (26)$$

Let us now compare the above equation with (25). Then, the following transfer function is chosen as an analog prototype filter:

$$G(s) = \frac{1}{1 + Ts}. \quad (27)$$

Thus, we obtain an IIR digital filter identical to filter (16). Next, the selected analog prototype filter $G(s)$ is discretized by the Tustin method. Thus, we can get $G[z]$, which is equal to (19).

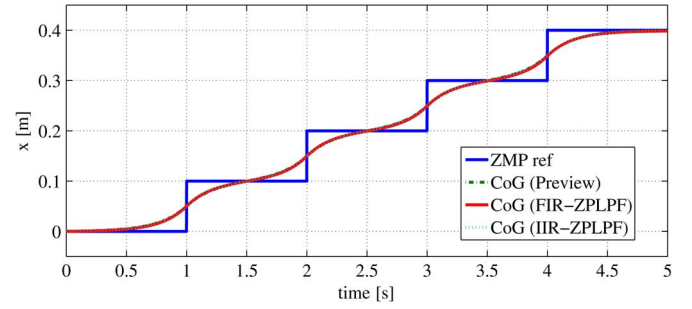


Fig. 9. Generated CoG trajectory.

F. Comparison of CoG Pattern Generation Methods

1) *Design Cost*: In the preview control approach, we need to solve the n th-order Riccati equation to calculate feedback gains and preview gains. In contrast to the ZPLPF approach, FIR-ZPLPF only needs to calculate the filter coefficient from the impulse response using (20)–(22). The IIR-ZPLPF only needs to calculate the Tustin conversion of (27). Thereby, the design cost of ZPLPF is much smaller than that of the preview control approach.

2) *Computational Processing*: The CoG trajectories generated by the preview control ZPLPF (FIR, IIR) are shown in Fig. 9. Here, we generate a 5-s CoG trajectory for the ZMP step reference under the condition that the sampling time is $\Delta t = 1$ ms and $M = 1200$. The average computation times over 100 runs for each method are 40.80, 44.12, and 0.2190 ms (CPU: Intel Pentium Dual Core 2.4 GHz). The computational processing involved in the preview control and that in FIR-ZPLPF are almost the same. Therefore, the advantages of the FIR-ZPLPF are the ease of theoretical development and implementation. The tap length M of the FIR-ZPLPF is large (e.g., in our case, the sum of the tap length of the causal and the noncausal filter is 2400). In contrast, the tap length of the IIR-ZPLPF is much smaller (the sum of the tap length of the causal and the noncausal filter is always 2). Thus, the IIR-ZPLPF is superior to the conventional approach in terms of computational time. However, the IIR-ZPLPF must use the FILO method. As a result, the IIR-ZPLPF is not suitable for sequential trajectory generation at each sampling time.

IV. WHOLE-BODY MOTION GENERATION: KINEMATIC RESOLUTION

A. Nonslippage Constraint for Wheel-Legged Mechanism [8]

In general, the kinematic constraints for WLMRs are based on the nonslippage assumption for each contact point. The slippage of contact points is described as follows:

$$\mathbf{v}_{s_i} = {}^w \dot{\mathbf{p}}_{c_i} - {}^w \mathbf{R}_{c_i} \begin{bmatrix} R\dot{\phi}_i \\ 0 \\ 0 \end{bmatrix} \quad (28)$$

where \mathbf{v}_{s_i} is the slippage of the i th leg and R is the wheel radius. The details of ${}^w \mathbf{R}_{c_i} = [\mathbf{t}_{c_i} \ \mathbf{l}_{c_i} \ \mathbf{n}_{c_i}]$ are shown in Fig. 4. Here, \mathbf{n}_{c_i} is the contact normal vector, \mathbf{t}_{c_i} is the longitudinal vector, and $\mathbf{l}_{c_i} = \mathbf{n}_{c_i} \times \mathbf{t}_{c_i}$ is the lateral vector. In this paper,

we assume that the ground surface is sufficiently flat and stiff. Therefore, \mathbf{n}_{c_i} becomes $[0 \ 0 \ 1]^T$. Then, \mathbf{t}_{c_i} is calculated as follows:

$$\mathbf{t}_{c_i} = \frac{\mathbf{z}_{\phi_i} \times \mathbf{n}_{c_i}}{|\mathbf{z}_{\phi_i} \times \mathbf{n}_{c_i}|} \quad (29)$$

where \mathbf{z}_{ϕ_i} is the rotational wheel axis vector. Thereafter, ${}^w\dot{\mathbf{p}}_{c_i}$ can be described on the basis of forward kinematics as follows:

$${}^w\mathbf{p}_{c_i} = {}^w\mathbf{p}_B + {}^w\mathbf{R}_B {}^B\mathbf{p}_{c_i} \quad (30)$$

$${}^w\dot{\mathbf{p}}_{c_i} = {}^w\dot{\mathbf{p}}_B + {}^w\dot{\mathbf{R}}_B {}^B\mathbf{p}_{c_i} + {}^w\mathbf{R}_B {}^B\dot{\mathbf{p}}_{c_i}. \quad (31)$$

Here, ${}^w\dot{\mathbf{R}}_B$ can be expressed as ${}^w\dot{\mathbf{R}}_B = {}^w\boldsymbol{\omega}_B^\wedge \cdot {}^w\mathbf{R}_B$. Then,

$$\begin{aligned} {}^w\dot{\mathbf{R}}_B {}^B\mathbf{p}_{c_i} &= {}^w\boldsymbol{\omega}_B^\wedge \cdot ({}^w\mathbf{R}_B {}^B\mathbf{p}_{c_i}) \\ &= -({}^w\mathbf{R}_B {}^B\mathbf{p}_{c_i})^\wedge \cdot {}^w\boldsymbol{\omega}_B \end{aligned} \quad (32)$$

$$= -({}^w\mathbf{R}_B {}^B\mathbf{p}_{c_i}) \times {}^w\boldsymbol{\omega}_B. \quad (33)$$

${}^B\dot{\mathbf{p}}_{c_i}$ can be described as

$${}^B\dot{\mathbf{p}}_{c_i} = \frac{\partial {}^B\mathbf{p}_{c_i}}{\partial \theta_{\text{leg}i}} \dot{\theta}_{\text{leg}i} = \mathbf{J}_{\text{leg}i} \dot{\theta}_{\text{leg}i} \quad (34)$$

where $\mathbf{J}_{\text{leg}i} \in \mathbb{R}^{3 \times 4}$ is the Jacobian matrix calculated as follows:

$$\mathbf{J}_{\text{leg}i} = [\mathbf{z}_{\theta_{1i}} \times \mathbf{a}_{\theta_{1i}} \ \mathbf{z}_{\theta_{2i}} \times \mathbf{a}_{\theta_{2i}} \ \mathbf{z}_{\theta_{3i}} \times \mathbf{a}_{\theta_{3i}} \ \mathbf{z}_{\theta_{4i}} \times \mathbf{a}_{\theta_{4i}}] \quad (35)$$

where \mathbf{z}_x is the rotation axis vector and $\mathbf{a}_x (= {}^B\mathbf{p}_{c_i} - {}^B\mathbf{p}_x)$ is the vector connecting each joint center to the corresponding leg contact point. Thus, (28) can be rearranged as follows:

$$\begin{aligned} \mathbf{v}_{s_i} &= {}^w\dot{\mathbf{p}}_B - ({}^w\mathbf{R}_B {}^B\mathbf{p}_{c_i}) \times {}^w\boldsymbol{\omega}_B \\ &\quad + {}^w\mathbf{R}_B \mathbf{J}_{\text{leg}i} \dot{\theta}_{\text{leg}i} - {}^w\mathbf{R}_{c_i} \begin{bmatrix} R\dot{\phi}_i \\ 0 \\ 0 \end{bmatrix}. \end{aligned} \quad (36)$$

In general, \mathbf{v}_{s_i} is set to $\mathbf{0}$ to prevent slippage. Then, to simplify the calculation, the above equation is multiplied by ${}^w\mathbf{R}_B^T$, yielding

$$\mathbf{0} = {}^w\mathbf{R}_B^T {}^w\dot{\mathbf{p}}_B - {}^B\mathbf{p}_{c_i} \times {}^w\boldsymbol{\omega}_B + \mathbf{J}_{\text{leg}i} \dot{\theta}_{\text{leg}i} - {}^B\mathbf{R}_{c_i} \begin{bmatrix} R\dot{\phi}_i \\ 0 \\ 0 \end{bmatrix}. \quad (37)$$

Then, (37) can be written in matrix form as follows:

$$\begin{aligned} \mathbf{0} &= [{}^w\mathbf{R}_B^T - {}^B\mathbf{p}_{c_i}^\wedge] \begin{bmatrix} {}^w\dot{\mathbf{p}}_B \\ {}^w\boldsymbol{\omega}_B \end{bmatrix} \\ &\quad + \left[\mathbf{J}_{\text{leg}i} - {}^B\mathbf{R}_{c_i} \begin{bmatrix} R \\ 0 \\ 0 \end{bmatrix} \right] \begin{bmatrix} \dot{\theta}_{\text{leg}i} \\ \dot{\phi}_i \end{bmatrix} \end{aligned} \quad (38)$$

$$= \mathbf{J}_{B_i}^{\text{slip}} \boldsymbol{\xi}_B + \mathbf{J}_{\theta_i}^{\text{slip}} \dot{\theta}_i = \begin{bmatrix} \mathbf{J}_{B_i}^{\text{slip}} & \mathbf{J}_{\theta_i}^{\text{slip}} \end{bmatrix} \begin{bmatrix} \boldsymbol{\xi}_B \\ \dot{\theta}_i \end{bmatrix}. \quad (39)$$

Subsequently, the leg constraint equations (k = total number of legs) are given by

$$\begin{bmatrix} 0 \\ 0 \\ \vdots \\ 0 \end{bmatrix} = \begin{bmatrix} \mathbf{J}_{B_1}^{\text{slip}} & \mathbf{J}_{\theta_1}^{\text{slip}} & \mathbf{0} & \cdots & \mathbf{0} \\ \mathbf{J}_{B_2}^{\text{slip}} & \mathbf{0} & \mathbf{J}_{\theta_2}^{\text{slip}} & & \mathbf{0} \\ \vdots & \vdots & & \ddots & \\ \mathbf{J}_{B_k}^{\text{slip}} & \mathbf{0} & \mathbf{0} & & \mathbf{J}_{\theta_k}^{\text{slip}} \end{bmatrix} \begin{bmatrix} \boldsymbol{\xi}_B \\ \dot{\theta}_1 \\ \dot{\theta}_2 \\ \vdots \\ \dot{\theta}_k \end{bmatrix} \quad (40)$$

$$\mathbf{0} = \mathbf{J}_{\text{slip}} \dot{\mathbf{q}} \quad (41)$$

where $\mathbf{J}_{B_i}^{\text{slip}} = [{}^w\mathbf{R}_B^T - {}^B\mathbf{p}_{c_i}^\wedge] \in \mathbb{R}^{3 \times 6}$, $\boldsymbol{\xi}_B = [{}^w\dot{\mathbf{p}}_B^T \ {}^w\boldsymbol{\omega}_B^T]^T \in \mathbb{R}^6$, $\mathbf{J}_i \in \mathbb{R}^{3 \times n}$, $\mathbf{J}_{\text{slip}} \in \mathbb{R}^{3k \times (6+kn)}$, and $\mathbf{q} \in \mathbb{R}^{kn}$.

B. Contact Point Constraint for ZMP-Based Wheeled Locomotion

In this section, the constraint for the contact point of each leg is defined. The objective is to constrain the ZMP at the center of the supporting polygon. To realize this, the initial posture of the robot is set to centralize the ZMP. In addition, the following constraint is imposed:

$$\begin{aligned} {}^w\dot{\mathbf{p}}_{\text{zmp}} &= {}^w\dot{\mathbf{p}}_{c_i} \\ &= {}^w\dot{\mathbf{p}}_B - ({}^w\mathbf{R}_B {}^B\mathbf{p}_{c_i}) \times {}^w\boldsymbol{\omega}_B + [{}^w\mathbf{R}_B {}^B\mathbf{J}_{\text{leg}i} \ \mathbf{0}] \dot{\theta}_i \\ &= \mathbf{J}_{B_i}^{\text{ZMP}} \boldsymbol{\xi}_B + \mathbf{J}_{\theta_i}^{\text{ZMP}} \dot{\theta}_i \\ &= \begin{bmatrix} \mathbf{J}_{B_i}^{\text{ZMP}} & \mathbf{J}_{\theta_i}^{\text{ZMP}} \end{bmatrix} \begin{bmatrix} \boldsymbol{\xi}_B \\ \dot{\theta}_i \end{bmatrix} \end{aligned} \quad (42)$$

where $\mathbf{J}_{B_i}^{\text{ZMP}} = [E \ -{}^w\mathbf{R}_B {}^B\mathbf{p}_{c_i}^\wedge] \in \mathbb{R}^{3 \times 6}$ and $\mathbf{J}_{\theta_i}^{\text{ZMP}} = [{}^w\mathbf{R}_B {}^B\mathbf{J}_{\text{leg}i} \ \mathbf{0}] \in \mathbb{R}^{3 \times n}$. By using this constraint, the ZMP is always set at the center of the supporting polygon. Thereafter, the leg constraint equations are described as follows:

$$\begin{bmatrix} {}^w\dot{\mathbf{p}}_{\text{zmp}} \\ {}^w\dot{\mathbf{p}}_{\text{zmp}} \\ \vdots \\ {}^w\dot{\mathbf{p}}_{\text{zmp}} \end{bmatrix} = \begin{bmatrix} \mathbf{J}_{B_1}^{\text{ZMP}} & \mathbf{J}_{\theta_1}^{\text{ZMP}} & \mathbf{0} & \cdots & \mathbf{0} \\ \mathbf{J}_{B_2}^{\text{ZMP}} & \mathbf{0} & \mathbf{J}_{\theta_2}^{\text{ZMP}} & & \mathbf{0} \\ \vdots & \vdots & & \ddots & \\ \mathbf{J}_{B_k}^{\text{ZMP}} & \mathbf{0} & \mathbf{0} & & \mathbf{J}_{\theta_k}^{\text{ZMP}} \end{bmatrix} \begin{bmatrix} \boldsymbol{\xi}_B \\ \dot{\theta}_1 \\ \dot{\theta}_2 \\ \vdots \\ \dot{\theta}_k \end{bmatrix} \quad (43)$$

$${}^w\bar{\mathbf{p}}_{\text{zmp}} = \mathbf{J}_{\text{zmp}} \dot{\mathbf{q}} \quad (44)$$

where ${}^w\bar{\mathbf{p}}_{\text{zmp}} = [{}^w\dot{\mathbf{p}}_{\text{zmp}}^T \ {}^w\dot{\mathbf{p}}_{\text{zmp}}^T \ \cdots \ {}^w\dot{\mathbf{p}}_{\text{zmp}}^T]^T \in \mathbb{R}^{3k}$ and $\mathbf{J}_{\text{zmp}} \in \mathbb{R}^{3k \times kn}$.

C. Momentum Jacobian

In general, the whole-body motion generation of a biped robot is achieved using an approximated LIP. The robot CoG pattern is planned on the basis of LIP. Then, the generated CoG pattern is distributed over the joint velocities by using the CoG Jacobian [26], [27]. In this section, the linear and the angular momentum Jacobian for the 3-D WLMR are derived. The linear momentum Jacobian includes the CoG Jacobian. Therefore, the desired robot CoG pattern can be realized using the linear momentum Jacobian. In addition, the angular momentum around the CoG of robot and joint velocities can be mapped using the angular momentum Jacobian. Thus, the

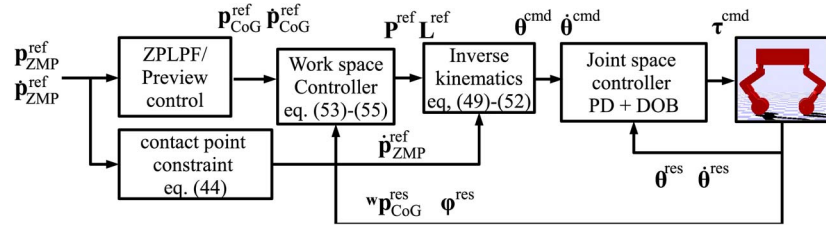


Fig. 10. Overall control block diagram.

desired angular momentum can be realized using the angular momentum Jacobian.

First, the linear and angular momentum equations are derived. The linear momentum and angular momentum around the CoG of the robot are described as follows:

$$\mathbf{P} = \sum_{i=1}^N m_i {}^w \dot{\mathbf{p}}_{G_i} \quad (45)$$

$$\mathbf{L} = \sum_{j=1}^N \mathbf{I}_i {}^w \boldsymbol{\omega}_i + ({}^w \mathbf{p}_{G_i} - \mathbf{p}_G) \times (m_i {}^w \dot{\mathbf{p}}_{G_i}) \quad (46)$$

where N is the total number of links and ${}^w \mathbf{p}_{G_i}$ is the CoG of the i th link. \mathbf{I}_i is the inertia of the i th link around its local origin. Then, (45) and (46) can be described in the following form:

$$\mathbf{P} = \mathbf{J}_P(\mathbf{q})\dot{\mathbf{q}} \quad (47)$$

$$\mathbf{L} = \mathbf{J}_L(\mathbf{q})\dot{\mathbf{q}} \quad (48)$$

where $\mathbf{J}_P(\mathbf{q})$ and $\mathbf{J}_L(\mathbf{q})$ are the linear and angular momentum Jacobians. \mathbf{J}_P and \mathbf{J}_L can be found in various studies. Fang and Pollard used the linear momentum Jacobian \mathbf{J}_P [33], and Morita and Ohnishi used the angular momentum Jacobian \mathbf{J}_L [34]. Kajita *et al.* called \mathbf{J}_P and \mathbf{J}_L the “inertia matrix” [30], while Orin *et al.* called them the “centroidal momentum matrix” [35]. In this paper, it is shown that the centroidal momentum matrix $\mathbf{A}_G = [\mathbf{J}_P^T \mathbf{J}_L^T]^T$ is the product of a pure inertia matrix and a pure Jacobian matrix. The derivations of \mathbf{J}_P and \mathbf{J}_L are also shown in these papers. Thereby, we can obtain the joint velocities which realize the desired momentum of the WLMR using (47) and (48).

D. Task Decomposition

In this section, we describe the task decomposition method and calculate the specific joint velocities that realize the desired whole body motion. The tasks defined in this paper are represented by (35), (40), (49), and (53). Here, the tasks are decomposed on the basis of the following task priorities considered in the inverse kinematics method [39]:

$$\dot{\mathbf{q}}^{cmd} = (\mathbf{I} - \mathbf{J}_{slip}^\dagger \mathbf{J}_{slip}) \dot{\mathbf{q}}_1 \quad (49)$$

$$\dot{\mathbf{q}}_1 = \mathbf{J}_P^\dagger \mathbf{P}^{ref} + (\mathbf{I} - \mathbf{J}_P^\dagger \mathbf{J}_P) \dot{\mathbf{q}}_2 \quad (50)$$

$$\dot{\mathbf{q}}_2 = \mathbf{J}_L^\dagger \mathbf{L}^{ref} + (\mathbf{I} - \mathbf{J}_L^\dagger \mathbf{J}_L) \dot{\mathbf{q}}_3 \quad (51)$$

$$\dot{\mathbf{q}}_3 = \mathbf{J}_{zmp}^\dagger {}^w \dot{\mathbf{p}}_{zmp}^{ref} \quad (52)$$

where \mathbf{J}^\dagger indicates the pseudoinverse of \mathbf{J} ($\mathbf{J}^\dagger = (\mathbf{J}^T \mathbf{J})^{-1} \mathbf{J}^T$). Thus, the desired linear momentum is realized on the condition

TABLE II
SIMULATION AND EXPERIMENTAL CONDITION

Contents	Simulation (ROCOS)	Experiment
Sampling time[ms] T_s	1.000	1.000
ZPLPF tap length M	1200	1200
Previewing period N_L	1200	1200
Q_e	1.000×10^6	1.000×10^6
Q_x	1.000	1.000
R	1.000	1.000
Height of CoG z_c [m]	0.464	0.464
Total mass m_{total}	47.0	47.0
\mathbf{K}_{pM}	$diag\{10.0, 10.0, 10.0\}$	$diag\{10.0, 10.0, 10.0\}$
\mathbf{K}_{pL}	$diag\{10.0, 10.0, 10.0\}$	$diag\{10.0, 10.0, 10.0\}$
Observer gains [rad/sec]		
-Crotch yaw	100.0	100.0
-Crotch roll	100.0	100.0
-Knee roll	100.0	100.0
-Shin yaw	100.0	100.0
-Wheel	100.0	100.0
PD gains for joints control (K_p, K_d)		
-Crotch yaw	(5.0, 1.0)	(5.0, 3.0)
-Crotch roll	(350.0, 50.0)	(25.0, 5.0)
-Knee roll	(200.0, 80.0)	(20.0, 5.0)
-Shin yaw	(10.0, 5.0)	(50.0, 5.0)
-Wheel	(10.0, 5.0)	(15.0, 5.0)

that the nonslippage constraint is achieved. In addition, the desired angular momentum and contact point constraint are realized using the remaining DoFs.

V. OVERALL CONTROL SYSTEM

To follow the position of the robot to the reference trajectory, a contact point and the CoG are controlled by a proportional controller described as follows:

$$\mathbf{P}^{ref} = m_{total} {}^w \dot{\mathbf{p}}_{CoG}^{ref} + \mathbf{K}_{pM} ({}^w \mathbf{p}_{CoG}^{ref} - {}^w \mathbf{p}_{CoG}^{res}) \quad (53)$$

where m_{total} is the total mass of the robot and \mathbf{K}_{pM} is the proportional controller gain. ${}^w \mathbf{p}_{CoG}^{ref}$ and ${}^w \mathbf{p}_{CoG}^{res}$ are the command and response positions of the CoG and each leg's contact point, respectively.

To control the posture of the robot to enable adaptation to uneven terrain, the reference angular momentum is generated as follows:

$$\mathbf{L}^{ref} = \mathbf{I}_n \boldsymbol{\omega}_B^{ref} \quad (54)$$

$$\boldsymbol{\omega}_B^{ref} = \mathbf{T}_\phi \mathbf{K}_{pL} (\phi^{cmd} - \phi^{res}) \quad (55)$$

where ϕ^{cmd} and ϕ^{res} are the commands and responses, respectively, and \mathbf{K}_{pL} is the proportional gain. \mathbf{T}_ϕ is the transformation matrix between $\boldsymbol{\omega}_B$ and $\dot{\phi}$.

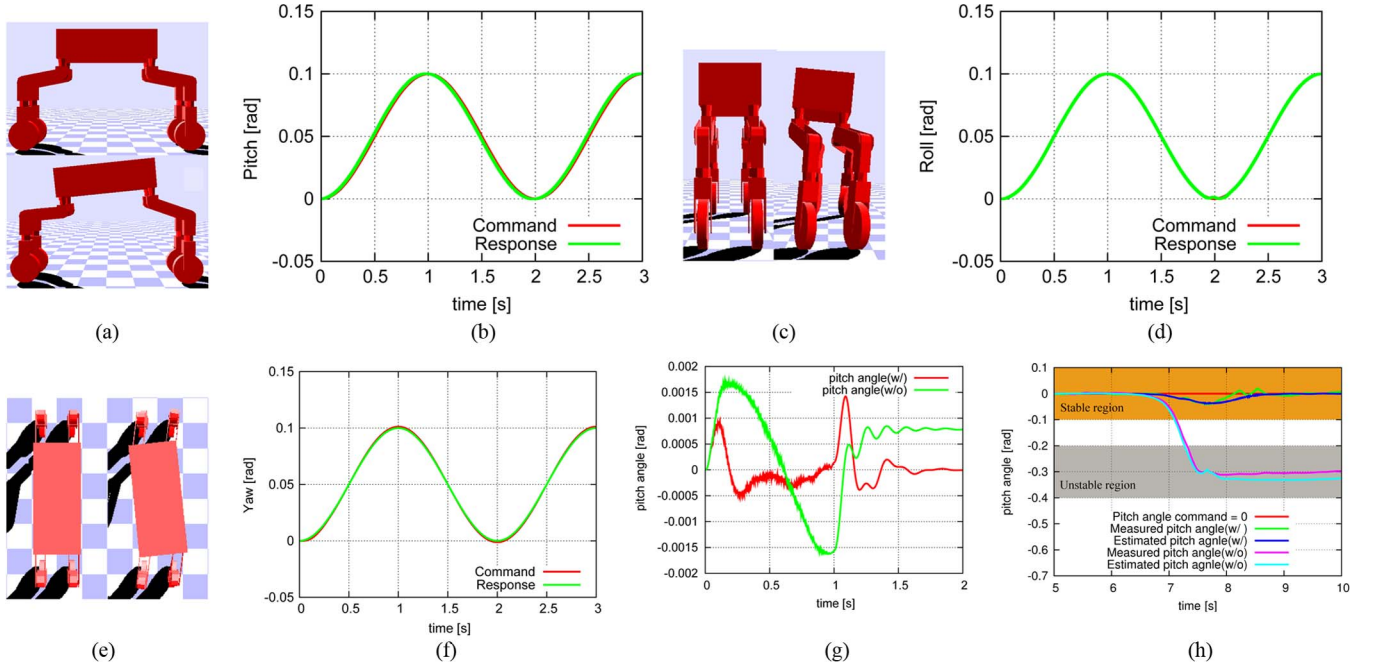


Fig. 11. Posture control results. (a) Environment. (b) Pitch angle response. (c) Environment. (d) Roll angle response. (e) Environment. (f) Yaw angle response. (g) Simulation: Pitching comparison. (h) Experiment: Pitching comparison.

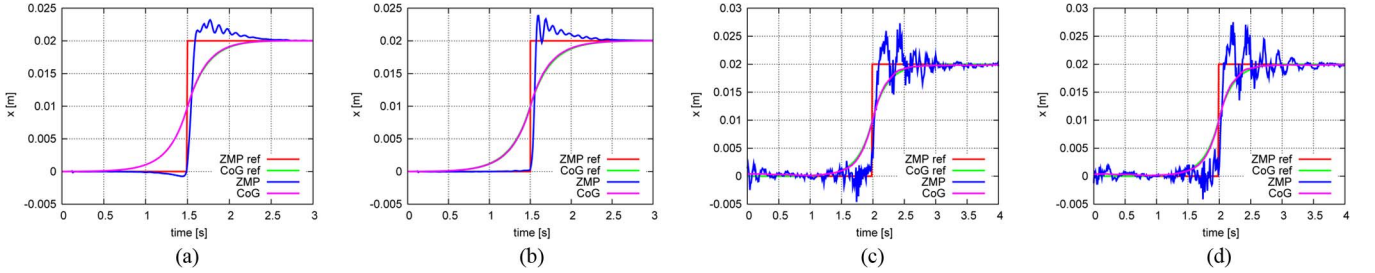


Fig. 12. Results of ZMP step response. (a) Simulation (preview control). (b) Simulation (ZPLPF). (c) Experiment (preview control). (d) Experiment (ZPLPF).

TABLE III
RMSE OF ZMP [IN MILLIMETERS]

Contents	Simulation (ROCOS)	Experiment
ZMP step response(zplpf)	2.445	2.014
ZMP step response(preview)	2.217	1.914
Wheeled locomotion(zplpf)	13.71	9.746
Wheeled locomotion(preview)	13.90	10.04
Gyrat. wheeled locomotion(zplpf)	4.886	10.90
Gyrat. wheeled locomotion(preview)	3.516	10.77

With these controllers, the reference momentum around the CoG is calculated. Thereafter, the joint velocities are calculated by the RMC scheme and then integrated to obtain the joint angles. Finally, the joints are controlled by the proportional derivative (PD) controller and disturbance observer [41]. The above control system is summarized in Fig. 10.

VI. SIMULATION AND EXPERIMENTAL RESULTS

In this section, the simulation and experimental results are shown. The simulations were conducted using the 3-D dynamical

simulator robot control simulator [42], and the experiments were conducted using the robot described in Fig. 1. The simulation and experimental condition is shown in Table II. To verify our proposed methods, (A) posture control, (B) ZMP step response, and (C) ZMP-based wheeled locomotion tests are conducted. Their details are shown in the following sections.

A. Results of Posture Control

First, the posture controller is validated by simulations and experiments. The results are shown in Fig. 11(a)–(h). Fig. 11(a)–(f) shows the simulation results of the roll, pitch, and yaw angle tracking. In this simulation, the robot posture is controlled to track the desired trajectory shown in the figures. The results show that our system can control the robot posture.

Fig. 11(g) and (h) shows the simulation and experimental results of the pitching control for carlike wheeled locomotion. Carlike wheeled locomotion means that the distance between the contact point of each leg and the origin of Σ_B is constant. The robot CoG is controlled to track the reference trajectory. In this case, the reference trajectory is given by a cosine function

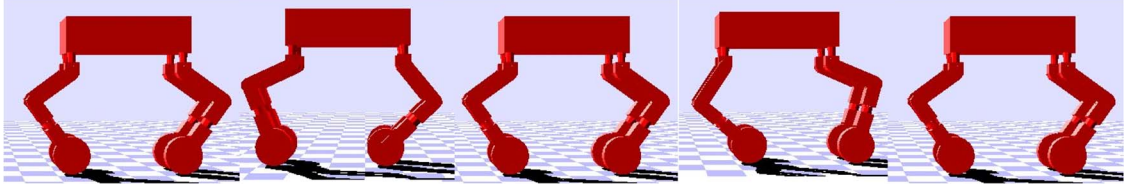


Fig. 13. Simulation environment (ZMP-based wheeled locomotion).



Fig. 14. Experimental environment (ZMP-based wheeled locomotion).

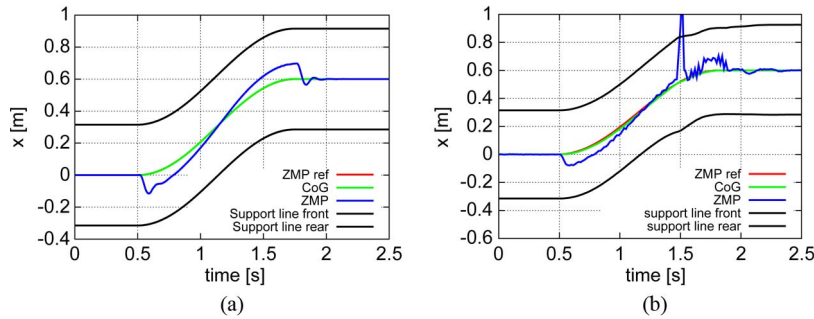


Fig. 15. Wheeled locomotion (without compensation: carlike). (a) Simulation result. (b) Experimental result.

such that the robot moves 1 m in the simulation and 0.6 m in the experiments during 1.5 s. The results show that the robot pitch angle is suppressed by the posture controller. Thus, the effectiveness of our posture controller for wheeled locomotion is validated.

B. Step Response of ZMP

In this section, we describe the simulation and experimental results of the ZMP step response. In the simulations and experiments, the control sampling time is 1 ms, the CoG height of the cart is 0.464 m, and $M = 1200$. The reference CoG trajectory generated by the preview control and ZPLPF is employed, and the CoG is controlled using the RMC scheme. Each contact point is fixed to the initial position. Here, the ZMP is calculated using the ZMP equation of a multilink model [40].

The simulation results are shown in Fig. 12(a) and (b), and the RMSE of the ZMP tracking is shown in Table III. The results show that some overshoots are present but that the actual ZMP follows the reference ZMP. Thus, when the CoG trajectory generated by the cart-table model approximated as a single point mass model is used, the actual ZMP follows the reference ZMP quite well.

Fig. 12(c) and (d) shows the experimental results of the ZMP step response with the proposed methods. In this figure, the actual ZMP follows the reference ZMP. Thus, the CoG trajectory generated by the proposed methods is the desired trajectory. The RMSE of the ZMP tracking result is shown in Table III. Here, experiments were conducted five times, and

an average of their RMSE is shown. The result is almost the same as that of the proposed methods. Thus, we can confirm the effectiveness of the control system based on the RMC scheme and the tracking performance of the proposed methods in the experiment.

C. ZMP-Based Wheeled Locomotion

1) *Without ZMP Compensation:* First, we show that the ZMP inverse response occurs when the robot moves like a car. The simulation and experimental results are shown in Fig. 15(a) and (b). In this case, the conditions of the simulation and experiment are the same as those for the pitching control shown in Fig. 11(g) and (h). From these results, we can confirm that the ZMP inverse response occurs and that the ZMP moves near the edge of the supporting polygon in both the simulation and experiment. In addition, the ZMP inverse response on the y component of ZMP is confirmed, as shown in Fig. 16(a) and (b). Here, the x component of the ZMP is controlled to track a constant value (0.6 m/s). The y component of the reference ZMP trajectory is given using the cosine function. The ZMP inverse response destabilizes the robot. Thus, to realize high mobility, this effect must be suppressed.

2) *With ZMP Compensation:* Here, the result of the control for wheeled locomotion is shown. The simulation and experimental environments of wheeled locomotion are shown in Figs. 13 and 14, respectively. In this control scheme, the robot CoG is controlled to follow the reference CoG generated by the preview control or ZPLPF by using (53). Each contact

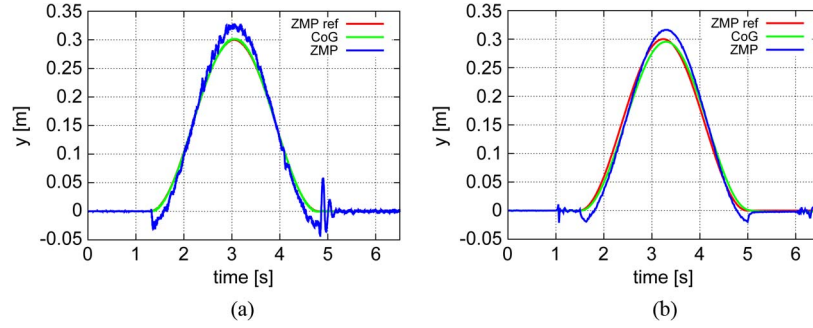


Fig. 16. Gyrating wheeled locomotion (without compensation: carlike). (a) Simulation result. (b) Experimental result.

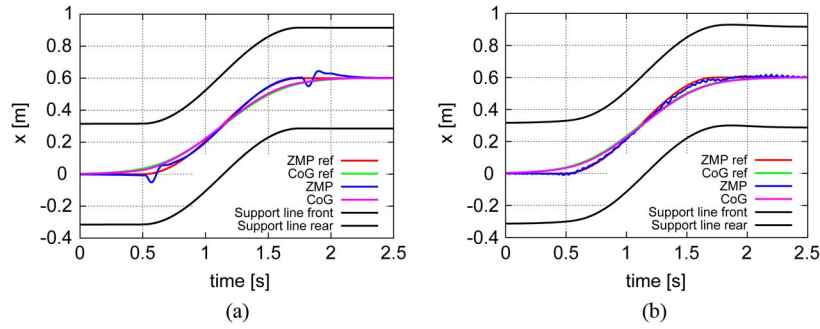


Fig. 17. Wheeled locomotion (with compensation: preview control). (a) Simulation result. (b) Experimental result.

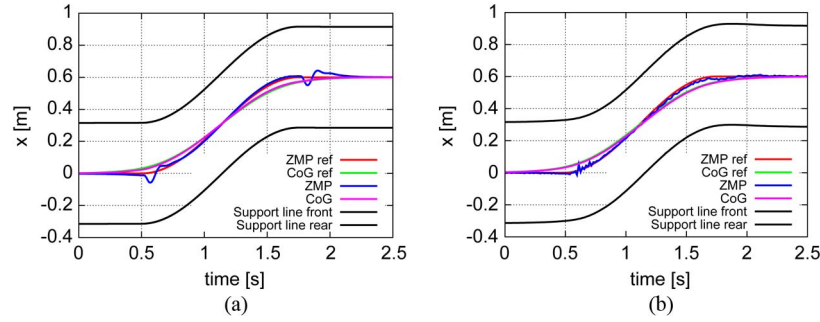


Fig. 18. Wheeled locomotion (with compensation: ZPLPF). (a) Simulation result. (b) Experimental result.

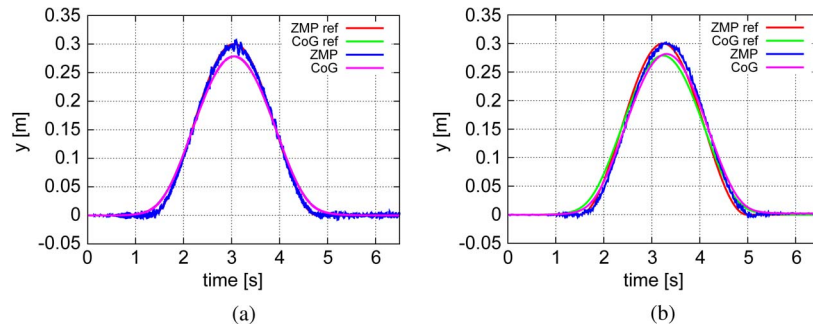


Fig. 19. Gyrating wheeled locomotion (with compensation: preview control). (a) Simulation result. (b) Experimental result.

point is constrained to centralize the ZMP inside the supporting polygon. Figs. 15, 16, 17(a), and 18(a) show the ZMP response of the wheeled locomotion evaluated with the proposed methods. The reference ZMP trajectory is given by a cosine function such that the robot moves 0.6 m during 1.25 s. In general, the inverse response of the ZMP occurs at the high position of the CoG. However, in this case, this is prevented by our control

system. From the figures, we can conclude that the proposed methods are also effective for fast-wheeled locomotion.

Figs. 17(b) and 18(b) show the experimental ZMP response. The reference ZMP trajectory is such that the robot moves 0.6 m during 1.25 s. Moreover, Figs. 19 and 20 show the validity of our methods for controlling the y component of ZMP. Here, the x component of ZMP is controlled to track a constant value

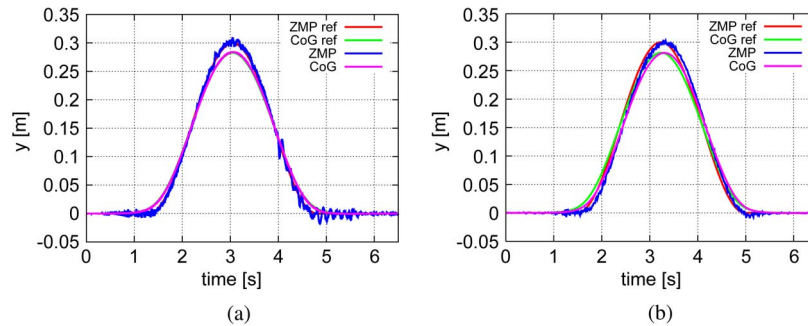


Fig. 20. Gyration wheeled locomotion (with compensation: ZPLPF). (a) Simulation result. (b) Experimental result.

(0.6 m/s). The y component of the reference ZMP trajectory is given using the cosine function. These figures show that the ZMP response of the robot can also be experimentally suppressed by the proposed methods. The RMSE of the ZMP tracking result is shown in Table III. Here, experiments were conducted five times, and an average of their RMSE is shown.

VII. CONCLUSION

In this paper, we proposed a ZMP-based whole body motion generation and control system to produce high mobility for a 3-D WLMR. Our contributions are as follows:

- 1) application of inverted pendulum model for WLMR;
- 2) CoG trajectory generation based on preview control;
- 3) CoG trajectory generation based on ZPLPF;
- 4) whole body motion generation based on RMC.

First, the 3-D WLMR was approximated as a single point mass LIP. Then, two control approaches were proposed: the preview control approach and a new CoG pattern generation method that realizes the desired ZMP using the ZPLPF. The ZPLPF approach can generate CoG patterns more easily than the preview control approach. The simplicity of the theory and implementation was verified by the design methods in Section III. In addition, the computational procedures were validated by performing a CoG pattern generation test. From this test, we conclude that the IIR-ZPLPF can generate the CoG pattern faster than the preview control approach. Next, the generated CoG pattern was realized by the linear momentum Jacobian, which includes the CoG Jacobian. In addition, the angular momentum Jacobian was introduced to further increase the mobility of the WLMRs. In this paper, the posture of the WLMR is controlled using the angular momentum as a control input. Finally, the generated CoG pattern and whole body motion generation scheme are validated by the ZMP step response and wheeled locomotion based on the ZMP. Furthermore, a ZMP-based wheeled locomotion method was proposed by manipulating the 3-D WLMR CoG and was validated. The proposed CoG pattern generation methods were validated via the aforementioned tests using the RMSE as an accuracy gauge. As a result, the ZMP errors of the proposed methods agree well in both simulation and experiment. Therefore, we can say that the ZPLPF approach is superior to the preview control approach in terms of implementation and computational processing.

REFERENCES

- [1] B. H. Wilcox, "ATHLETE: A cargo and habitat transporter for the moon," in *Proc. IEEE Aerosp. Conf.*, 2009, pp. 1–7.
- [2] S. Hirose and T. Hiroki, "Study on roller-walk-adaptation of characteristics of the propulsion by a leg trajectory," in *Proc. IEEE ICRA*, 2008, pp. 1532–1537.
- [3] Y. J. Dai, E. Nakano, T. Takahashi, and H. Okubo, "Motion control of leg-wheel robot for an unexplored outdoor environment," in *Proc. IEEE/RSJ IROS*, 1998, pp. 402–409.
- [4] H. Adachi, N. Koyachi, T. Arai, A. Shimizu, and Y. Nogami, "Mechanism and control of a leg-wheel hybrid mobile robot," in *Proc. IEEE ICRA*, 1999, pp. 1792–1797.
- [5] J. Smith, I. Sharf, and M. Trentini, "PAW: A hybrid wheeled-leg robot," in *Proc. IEEE ICRA*, 2006, pp. 4043–4048.
- [6] S. Moosavian and A. Mozdbaran, "Dynamics and motion planning of a wheel-legged mobile robot," in *Proc. IEEE CCA*, 2007, pp. 581–586.
- [7] A. Halme, I. Leppanen, S. Salmi, and S. Ylonen, "Hybrid locomotion of a wheel-legged machine," in *Proc. Int. Conf. Climbing Walking Robots*, 2000, pp. 167–174.
- [8] C. Grand, F. Benamar, and F. Plumet, "Motion kinematics analysis of wheeled-legged rover over 3D surface with posture adaptation," *Int. J. Mech. Mach. Theory*, vol. 45, no. 3, pp. 477–495, Mar. 2010.
- [9] T. Thomson, I. Sharf, and B. Beckman, "Kinematic control and posture optimization of a redundantly actuated quadruped robot," in *Proc. ICRA*, 2012, pp. 1895–1900.
- [10] P. R. Giordano, M. Fuchs, A. Albu-Schaffer, and G. Hirzinger, "On the kinematic modeling and control of a mobile platform equipped with steering wheels and movable legs," in *Proc. IEEE ICRA*, 2009, pp. 4080–4087.
- [11] T. Yoshioka, T. Takubo, T. Arai, and K. Inoue, "Hybrid locomotion of leg-wheel ASTERISK H," *J. Robot. Mechatron.*, vol. 20, no. 3, pp. 403–412, 2008.
- [12] S. Nakajima, "RT-Mover: A rough terrain mobile robot with a simple leg-wheel hybrid mechanism," *Int. J. Robot. Res.*, vol. 30, no. 13, pp. 1609–1626, Nov. 2011.
- [13] S. An, Y. Oh, and D. S. Kwon, "Zero-moment point based balance control of leg-wheel hybrid structures with inequality constraints of kinodynamic behavior," in *Proc. IEEE/RSJ IROS*, 2012, pp. 2471–2477.
- [14] B. Jensen, N. Tomatis, L. Mayor, A. Drygajlo, and R. Siegwart, "Robot meet humans—Interaction in public spaces," *IEEE Trans. Ind. Electron.*, vol. 52, no. 6, pp. 1530–1546, Dec. 2005.
- [15] K. Morioka, L. Joo-Ho, and H. Hashimoto, "Human-following mobile robot in a distributed intelligent sensor network," *IEEE Trans. Ind. Electron.*, vol. 51, no. 1, pp. 229–237, Feb. 2004.
- [16] A. Suzumura and Y. Fujimoto, "High mobility control for a wheel-legged mobile robot based on resolved momentum control," in *Proc. IEEE AMC*, 2012, pp. 1–6.
- [17] A. Suzumura and Y. Fujimoto, "Control of dynamic locomotion for the hybrid wheel-legged robot by using unstable-zeros cancellation," in *Proc. IEEE ICRA*, 2012, pp. 2337–2342.
- [18] M. Vukobratovic and B. Borovac, "Zero-moment point—Thirty five years of its life," *Int. J. Humanoid Robot.*, vol. 1, no. 1, pp. 157–173, 2004.
- [19] K. Erbaturo and O. Kurt, "Natural ZMP trajectories for biped robot reference generation," *IEEE Trans. Ind. Electron.*, vol. 56, no. 3, pp. 835–845, Mar. 2009.
- [20] N. Motoi, T. Suzuki, and K. Ohnishi, "A bipedal locomotion planning based on virtual linear inverted pendulum mode," *IEEE Trans. Ind. Electron.*, vol. 56, no. 1, pp. 54–61, Jan. 2009.

- [21] M. Krid and F. Benamar, "Design and control of an active anti-roll system for a fast rover," in *Proc. IEEE/RSJ IROS*, 2011, pp. 274–279.
- [22] S. Lee, M. Leibold, M. Buss, and F. Park, "Online stability compensation of mobile manipulators using recursive calculation of ZMP gradients," in *Proc. IEEE ICRA*, 2012, pp. 850–855.
- [23] D. Choi and J. Oh, "ZMP stabilization of rapid mobile manipulator," in *Proc. IEEE ICRA*, 2012, pp. 883–888.
- [24] S. Kajita, F. Kanehiro, K. Kaneko, K. Fujiwara, K. Harada, K. Yokoi, and H. Hirukawa, "Biped walking pattern generation by using preview control of zero-moment point," in *Proc. IEEE ICRA*, 2003, pp. 1620–1626.
- [25] S. Shimmyo, T. Sato, and K. Ohnishi, "Biped walking pattern generation by using preview control based on three-mass model," *IEEE Trans. Ind. Electron.*, vol. 60, no. 11, pp. 5137–5147, Nov. 2013.
- [26] T. Sugihara and Y. Nakamura, "Whole-body cooperative balancing of humanoid robot using COG Jacobian," in *Proc. IEEE/RSJ IROS*, 2002, vol. 3, pp. 2575–2580.
- [27] Y. Choi, D. Kim, Y. Oh, and B. You, "Posture/walking control for humanoid robot based on kinematic resolution of CoM Jacobian with embedded motion," *IEEE Trans. Robot.*, vol. 23, no. 6, pp. 1285–1293, Dec. 2007.
- [28] S. Kajita, M. Morisawa, K. Miura, S. Nakaoka, K. Harada, K. Kaneko, F. Kanehiro, and K. Yokoi, "Biped walking stabilization based on linear inverted pendulum tracking," in *Proc. IEEE/RSJ IROS*, 2010, pp. 4489–4496.
- [29] K. Löffler, M. Gienger, F. Pfeiffer, and H. Ulbrich, "Sensors and control concept of a biped robot," *IEEE Trans. Ind. Electron.*, vol. 51, no. 5, pp. 972–980, Oct. 2004.
- [30] S. Kajita, F. Kanehiro, K. Kaneko, K. Fujiwara, K. Harada, K. Yokoi, and H. Hirukawa, "Resolved momentum control: Humanoid motion planning based on the linear and angular momentum," in *Proc. IEEE/RSJ IROS*, 2003, vol. 2, pp. 1644–1650.
- [31] A. Goswami and V. Kalle, "Rate of change of angular momentum and balance maintenance of biped robots," in *Proc. IEEE ICRA*, 2004, vol. 4, pp. 3785–3790.
- [32] A. Macchietto, V. Zordan, and C. R. Shelton, "Momentum control for balance," *ACM Trans. Graphics*, vol. 28, no. 3, p. 80, Aug. 2009.
- [33] A. C. Fang and N. Pollard, "Efficient synthesis of physically valid human motion," *ACM Trans. Graphics*, vol. 22, no. 3, pp. 417–426, Jul. 2003.
- [34] Y. Morita and K. Ohnishi, "Attitude control of hopping robot using angular momentum," in *Proc. IEEE ICIT*, 2003, vol. 1, pp. 173–178.
- [35] D. E. Orin, A. Goswami, and S.-H. Lee, "Centroidal dynamics of a humanoid robot," *J. Auton. Robots*, vol. 35, no. 2/3, pp. 161–176, Oct. 2013.
- [36] T. Shiraishi and H. Fujimoto, "Trajectory tracking control method based on zero-phase minimum-phase factorization for nonminimum-phase continuous-time system," in *Proc. IEEE AMC*, 2012, pp. 1–6.
- [37] C. J. Kempf and S. Kobayashi, "Disturbance observer and feedforward design for a high-speed direct-drive positioning table," *IEEE Trans. Contr. Syst. Tech.*, vol. 7, no. 5, pp. 513–526, Sep. 1999.
- [38] L. R. Rabiner and B. Gold, *Theory and Application of Digital Signal Processing*. Englewood Cliffs, NJ, USA: Prentice-Hall, 1975.
- [39] Y. Nakamura, H. Hanafusa, and T. Yoshikawa, "Task priority based redundancy control of robot manipulators," *Int. J. Robot. Res.*, vol. 6, no. 2, pp. 3–15, Jun. 1987.
- [40] A. Takanishi, M. Ishida, Y. Yamazaki, and I. Kato, "The realization of dynamic walking by the biped walking robot," in *Proc. IEEE ICRA*, 1985, pp. 459–466.
- [41] K. Ohnishi, M. Shibata, and T. Murakami, "Motion control for advanced mechatronics," *IEEE/ASME Trans. Mechatronics*, vol. 1, no. 1, pp. 56–67, Mar. 1996.
- [42] Y. Fujimoto and A. Kawamura, "Simulation of an autonomous biped walking robot including environmental force interaction," *IEEE Robot. Autom. Mag.*, vol. 5, no. 2, pp. 33–42, Jun. 1998.



Akihiro Suzumura received the B.E. and M.E. degrees in electrical and computer engineering from Yokohama National University, Yokohama, Japan, in 2011 and 2013, respectively.

Since 2013, he has been with Denso Corporation, Ltd., Aichi, Japan. His research interests include robotics, manufacturing automation, and motion control.

Mr. Suzumura is a member of the Robotics Society of Japan.



Yasutaka Fujimoto (S'93–M'98–SM'12) received the B.E., M.E., and Ph.D. degrees in electrical and computer engineering from Yokohama National University, Yokohama, Japan, in 1993, 1995, and 1998, respectively.

In 1998, he joined the Department of Electrical Engineering, Keio University, Yokohama, as a Research Associate. Since 1999, he has been with the Department of Electrical and Computer Engineering, Yokohama National University, where he is currently a Professor. His research interests include actuators,

robotics, manufacturing automation, and motion control.

Dr. Fujimoto is the Chair of the IEEE Industrial Electronics Society Technical Committee on Sensors and Actuators (2012–2013), and a member of the Institute of Electrical Engineers of Japan, and the Robotics Society of Japan.